Volume 14, Issue 4, 142440 (1-17)

Iranian Journal of Catalysis (IJC)

https://doi.org/10.57647/j.ijc.2024.1404.40

Anatase- Brookite mixed phase TiO_2 nanoparticles for the photocatalytic degradation of methylene blue

M. S. Monisha, R. Sreeja *

Nanophotonics Laboratory, Department of Physics, Mar Ivanios College (Autonomous), Thiruvananthapuram, Kerala, India.

***Corresponding author:** sreeja.r@mic.ac.in

Original Research

Received:
31 January 2024
Revised:
31 August 2024
Accepted:
22 September 2024
Published online:
8 October 2024

Abstract:

Herein, we report visible light active, efficient, simple, bi-phasic photocatalyst composed of anatase-brookite mixed phase, crystalline TiO_2 nanoparticles synthesized through a simple sol-gel approach. The physicochemical characteristics of the nanoparticles were established through characterization tools such as XRD, FESEM, EDS, TEM, DRS, FT-IR, XPS, Raman, PL, and TGA. Visible light-driven degradation of methylene blue (MB) dye was observed, which was confirmed through the improvement in the rate constant compared to that in UV exposure. This can be attributed to the prolonged charge separation resulting from the anatase-brookite junction effect. The free radicals generated (superoxide anions and hydroxyl radicals) after the incidence of light are responsible for the photocatalytic degradation of the MB, whose influence was validated through the scavenger method. The generation of degradation intermediates were verified through LC-MS-MS analysis. The nanoparticles showed maximum photocatalytic performance in the basic pH conditions. The recyclability of the photocatalyst was also established. The enhanced activity resulting from the combined effect of anatase-brookite phases of TiO_2 in the nanoformulation will enable its potential use as a vital, visible light active, eco-friendly bi-phasic photo catalyst offering low-cost environment remediation in a short period of time using the minimum quantity of photocatalyst.

Keywords: Anatase- brookite mixed phase; Methylene Blue; Photocatalysis; TiO_2 nanoparticles; Sol-gel method

1. Introduction

The chemical contaminants from industry impose potential hazards to living organisms, and the effective degradation of these pollutants, either by natural or conventional means, is a global challenge. The majority of them will induce heavy hazards to living organisms and are harmful to the natural balance of our environment as these pollutants are toxic, mutagenic, and carcinogenic. Among the chemical pollutants, organic dyes stand out as the worst contaminant of water; more than 95% of the dye wastewater is produced by the food industry, chemical industry, and textile industry. It is a fact that around 7×10^5 metric tonnes of synthetic dyes are synthesized every year, and more than 100,000 dyes are commercially available. With the increasing demand for such dyeing compounds, more and more water resources are getting contaminated day by day [1]. In this context, the synthesis of efficient materials capable of abatement of these dye-based contaminants is a global need. There are a number of practical challenges for the effective removal of these contaminants, such as the lack of space, the need for heavy or expensive equipment, and complex procedures; some methods are either slow or non-destructive to some or most persistent organic pollutants, the presence of toxic byproduct, etc. In this scenario, solar photocatalysis using semiconductor oxides has been introduced as a highly efficient, inexpensive, eco-friendly, sustainable oxidation method offering potential functionality against these toxic contaminants in water or air. In photocatalysis, when a semiconducting material (Photocatalyst) is irradiated by light (usually in the UV and Visible region) of energy equal to or greater than the band gap (E_g), the photocatalyst absorbs

light, then electron-hole (e^-/h^+) pairs will be generated in the photocatalyst through photo induction, followed by the separation of charge carriers (holes move to valence band and electrons to the conduction band). Finally, the separated electrons and holes will directly or indirectly initiate redox reactions in such a way that oxidation happens in the conduction band and reduction happens in the valence band [2, 3], resulting in the degradation of pollutant species. Among the different semiconductor photocatalysts, Titanium dioxide (TiO_2) based systems have attracted significant scientific interest due to their distinctive properties such as excellent catalytic activity, oxidizing potential, large surface area, wide band gap energy, non-toxicity, biocompatibility, ecofriendly nature, high dielectric constant, and chemical stability, etc. Most importantly, it is an inexpensive material due to its low production cost, as it can be prepared using diverse procedures such as solution and gas phase methods.

Recently, a number of synthesis routes have been reported for the synthesis of TiO_2 nanoparticles and their dye degradation applications. Meselhy et al. reported autocombustion synthesis of lanthanum-doped TiO_2 nanostructures for the efficient photocatalytic degradation of crystal violet dye [4]. Yousef et al. reported the photocatalytic behavior of the hydrothermally synthesized urchin-shaped titanium dioxide nanoparticles utilizing methylene blue dye [5]. Nassar et al. prepared TiO_2 adsorbent via auto combustion method to be used as a promising candidate for the removal of RR195 textile dye from water [6]. Also, Andrade Guel et al. developed TiO_2 nanoparticles by microwave-assisted sol-gel technique [7]. Pure TiO_2 thin films were synthesized through chemical vapor deposition by Alotaibi et al. for photocatalytic applications [8]. Honda et al. reported Cu-doped TiO_2 (Cu-TiO_2) structures based on the liquid phase deposition method [9]. But out of all these reported techniques, the sol-gel method has been observed to be the most preferred choice for synthesizing TiO_2 nanoparticles as it offers several advantages such as greater morphological control, ease of synthesis, low-temperature requirement, and a short period of reaction time [10]. However, the sol-gel-derived TiO_2 nanoparticles exhibit broad size distribution and particle agglomeration, which reduces their chances of being used in many potential applications. In order to overcome these critical issues during the nanoparticle synthesis, the pre-and post-synthetic conditions like proportionate use of chemicals, annealing temperature, the ratio between solvent and distilled water, reaction time, and reaction temperature can be recorded and fixed accurately along with the timely monitoring during separation and washing of nanoparticles, so as to achieve the desired nature of the particles [11, 12]. But TiO_2 exhibits some drawbacks like all semiconductor oxide materials; fast charge carrier recombination, photo corrosion, and long reaction time are the significant factors that reduce the photoactivity of semiconductor oxide-based photocatalysts in general [13]. Numerous efforts were taken by the scientific community to reduce such limitations offered by the semiconductor oxide based photocatalysts. Dhull et al. developed doped InVO4-based hetero junction systems to avoid the potential limitations of the pure InVO4 systems, like its less harvest of solar energy resulting from the slow migration and separation of photoinduced charge carriers [14]. Bembibre et al. used the joined effect of photocatalysis and sonocatalysis by irradiating a semiconductor with acoustic waves to generate free radicals and increase photo-oxidation of organic pollutants, thereby improving photocatalytic efficiency [15]. Also, MnO_2 based composites were reported recently as having higher catalytic efficiency due to their hetero junction structure with other materials [2]. But instead of going to employ composite type hetero junction systems and complex or multiple photocatalytic methods, it is better and cost effective to modify the conventional photocatalyst TiO_2 in a more adaptable and effective manner. This can be achieved by suitably tuning the particle size, crystallinity, and phase of the photocatalytic semiconductor oxide materials, through which most of the potential limitations can be mitigated.

TiO_2 exists in three prominent crystalline phases, namely anatase, brookite, and rutile. Among all phases, the highest photocatalytic efficiency was displayed by the anatase phase, whereas the rutile phase shows a low photocatalytic response and usually displays no response in the brookite phase [16–18]. Generally, the anatase phase occupies a superior position for applications such as photocatalysis, photoelectron chemistry, drug delivery, optical and optoelectronic devices, photovoltaic cells, sensors, antibacterial technology owing to its large photochemical stability, small crystallite size, photo-generated electrons with higher potential energy, strong oxidizing potential, and non-toxicity, etc. [19–21]. The larger band gap of anatase (3.2 eV) can elevate the valence band maximum to higher energy levels compared to the redox potentials of surface-adsorbed pollutant molecules [22].This will, in turn, enhance the oxidation potential of electrons, thereby facilitating the transfer of electrons from TiO_2 to the surface-adsorbed molecules. In spite of these novel properties, anatase phase face some shortcomings associated with a large band gap, making it less efficient in the visible spectral range limiting its efficient use to the ultra violet region only. Also, the fast recombination of electron and hole pair makes them unsuitable for the complete removal of the dye. As the single phase, TiO_2 faces these potential limitations resulting from the accumulation of electrons in the conduction band, leading to the recombination of the photo-excited electron-hole pairs affecting its catalytic performance; the consequence of mixed-phase on the photocatalytic performance is to be evaluated as the improved photocatalytic response results from the combined effect of the mixed phases compared to the single phase. There are a number of reports on the relevance of mixed-phase of TiO_2 nanoparticles for photocatalytic applications. Szoldra et al. reported that smaller symmetry and band-gap value close to the anatase phase enable the brookite phase to have very good photocatalytic capacities, thus making the anatase-brookite phase TiO_2 nanoparticles a potential heterogeneous photocatalyst [23]. According to the observation of Ismail et al., the photocatalytic enhancement in brookite nanorods was attributed to the shift of flat band potential in the brookite phase more cathodically compared to the anatase phase and due to the phenomenon of better

charge carrier separation in anatase-brookite mixed phases [24]. Yu et al. have observed a very similar result that the sol-gel derived anatase–brookite mixed phase nanoparticles exhibit higher photocatalytic efficiency as compared to the pure anatase phase [25]. Toshiaki Ozawa has performed the low-temperature synthesis of anatase–brookite mixed-phase nanoparticles and studied the junction effect among different phases on the photocatalytic performance [26]. The high photo response of mixed phases of TiO_2 owes to the enhanced separation of the photogenerated electron-hole pairs (thereby obstructing their recombination) due to the existence of junctions among various phases [27]. Prolonged charge separation (e^-/h^+) caused by such a unique combination of phases promotes the likelihood of charge carriers in engaging the surface reactions followed by the rapid generation of reactive oxygen species such as superoxide anions (O^{2-}) and hydroxyl radicals (OH^*) that photo decomposes the organic dyes. Thus, in order to enhance the photoactivity of the TiO_2 photocatalyst, the anatase - brookite mixed phase of the TiO_2 in a nanoformulation has been fabricated here using the sol-gel method as it is a simple, cost-effective method allowing higher crystallinity to the nanoparticles. Also, this mixed-phase photocatalyst has been employed for the photocatalytic degradation of Methylene blue dye, which is an environmentally persistent, toxic, carcinogenic, and mutagenic dye [28]. This common synthetic dye has been used in textile, paper, and leather industries, and hence, it is quite essential to remove the dye from industrial wastewater as its dosage in surface and groundwater may challenge the existence of fauna and aquatic ecosystems and may even cause serotonin toxicity in human beings. In this scenario, this novel mixed-phase photocatalyst and its applicability thus hold great promise to tackle current and future industrial dye removal challenges causing minimum environmental damage.

2. Experimental

2.1 Materials and methods

The metal precursor used for the synthesis of TiO_2 nanoparticles is Titanium (IV) isopropoxide (99%, SRL), 2-Propanol (99.5%, SRL) function as the solvent and the alkoxide hydrolysis is performed by distilled water. Commercially available bulk anatase phase TiO_2 (Sigma Aldrich 99%) was used for a comparison.

2.1.1 Synthesis of TiO_2 nanoparticles

For the synthesis of the TiO_2 nanoparticles, 14.952 mL of TTIP was dissolved in 100 mL of 2-Propanol, and it was stirred for 15 min (1200 rpm, REMI) at room temperature [29]. Subsequently, 30 mL of distilled water was added to the TTIP solution, and the mixture was further allowed to stir for the next 30 minutes. The obtained solution was centrifuged (REMI) at a speed of 10000 rpm (at 20 ^oC) to get a white precipitate, and it was washed with distilled water and acetone thrice. The final washed precipitate was dried well employing a hot air oven (KEMI) at 150 ^oC for 1 h. The dried powder was crushed and calcined using a muffle furnace at 500 ^oC for 2 h. Further, the calcined powder was ground well using agate mortar for 30 min and was used for further experiments.

2.1.2 Photocatalytic studies

The photocatalytic response of TiO_2 nanoparticles was investigated through the evaluation of the degradation of Methylene blue dye under UV light, natural visible light, and dark conditions. In each experiment, the photocatalyst TiO_2 nanoparticles (20 mg, 40 mg and 60 mg) was dispersed in 100 mL of 0.05 mM aqueous dye solution and it is continuously stirred for 15min in dark condition in order to attain adsorption-desorption equilibrium. Then the solution was transferred to beakers and then placed in artificial UV light, natural sunlight, and dark. The decomposition of the dye (Methylene blue) was estimated using the Schimadzu UV 170 Spectrophotometer by recording the absorption peak of Methylene blue at a wavelength of 664 nm by taking 5mL irradiated MB solution every 20 min for 200 minutes. Photocatalytic experiments were done repeatedly by varying the concentration of TiO_2 nanoparticles (photocatalyst) and dye concentrations. All the above experiments were done at ambient temperature in the months of September to November. The intermediate products during photocatalysis were analyzed using LC-MS-MS spectrometry (Shimadzu LC-MS-MS 8045), where different species were detected based on their m/z values. For that, the mixed solution (MB+TiO_2) after the complete decoloration of MB was centrifuged, and then the supernatant solution was collected. Then LC-MS-MS spectra the supernatant solution was taken to analyse the presence of disintegration intermediates. The scavenger method can be used to establish the role of free radicals on photocatalytic efficiency, which is based on the sudden decrease in dye degradation after the addition of a specific scavenger species. In this work, we have employed specific scavengers of various active species such as $OH^\star$,h^+,e^-,and $*O_2{}^-$. 1 mL of 1 mM Disodium Ethylene diamine tetra acetate, ascorbic acid, $AgNO_3$, and Tert butyl alcohol were used as scavengers added to the photocatalyst material in order to capture holes (h^+), superoxide radicals ($*O^{2-}$.), electrons (e^-) and hydroxyl radicals ($OH^\star$) respectively. Since the stability of the photocatalyst is very relevant from an industrial perspective, the recyclability of the photocatalyst after the degradation of the dye will be evaluated after every use. For this, the MB solution treated with the photocatalyst has undergone centrifugation at 12000 rpm after degradation followed by washing with ethanol three times and drying at 80 ^oC for 3 hr in a hot air oven. The pH dependence of the photocatalytic degradation rate was also checked by varying the pH of the solution (from 3 to 11) by adding dilute HCl (10 mL HCl in 20 mL water) or aqueous NaOH solution (0.4 M) dropwise.

2.2 Characterization of TiO_2 nanoparticles

The crystal structure, phase, and chemical composition of the nanoparticles were evaluated using X-ray powder diffraction (XRD) [Bruker AXS D8 ADVANCE X-ray diffractometer with DAVINCI design of CuKα radiation (λ=1.5406^{o}A) with 2θ in the range of 10^o to 80^o]. The thermal gravimetric analysis of nanoparticles is done by the simultaneous thermal analyzer (TGDTA/DSC) [PerkinElmer STA 8000]. The surface morphology and particle size were

identified by Field Emission Scanning Electron Microscopy (FESEM) [FEI Thermo Fisher Nova Nano SEM 450]. An energy-dispersive X-ray analyzer (EDX) was used [Carl Zeiss EVO 18 Research] to find out the chemical composition of TiO_2 nanoparticles. The homogeneity and size of the particles were confirmed through Transmission electron microscopy (Jeol/JEM 2100) measurements. The crystal planes of the nanoparticles were confirmed from the SAED patterns. The optical characteristics of the samples were evaluated using UV-Vis absorption studies [Agilent technologies carry 5000] in the range of 200 to 700 nm. Fourier Transform Infrared Spectrophotometer (FT-IR) [Thermoscientific NicoletiS50] was used to study the vibrational bands and functional groups of the material in the range 4000 cm^{-1} to 400 cm^{-1}. A sophisticated Fluorescence Spectrometer (SFS) [Edinburgh FLS 1000-SS-sm] was used for the study of photoluminescent emission properties of synthesized samples. X-ray Photoelectron Spectrometer (XPS) [Thermo Scientific TM ESCALAB TM Xi+] was used for measuring the elemental composition as well as for determining the binding energy states of different elements, and the band edge positions were determined from the Valence band XPS. The vibrational energy modes of the nanoparticles were evaluated using a Micro Raman analyzer [Imaging spectrograph STR 500mm], in which the source of excitation was the He-Ne laser.

3. Results and discussion

3.1 XRD analysis

Figure 1 depicts the X-ray diffraction patterns of synthesized TiO_2 nanoparticles, which are compared with those of commercially available bulk anatase phase TiO_2. The diffraction peaks of the nanoparticles corresponding to 2θ values of 25.27° (101), 37.83° (004), 47.98° (200), 53.96° (105), 55° (211), 62.68° (204), 68.87° (220), 70.26° (220) and 75.15° (215) confirm the anatase phase having a tetragonal structure which matches well with JCPDS File No. 21-1272 (Space Group -$I_{41/amd}$) [30]. A very small peak at 30.73° (121) is due to the brookite phase of TiO_2 [31], as confirmed by JCPDS File No. 29-1360 (Space Group -pbca). The displayed XRD patterns of TiO_2 confirm the intense peak of the anatase phase at the 25.27° (101) plane. Using the equation 1, the lattice parameters were obtained to be a=b=3.7884 Å and c=9.5044 Å [32]. The average particle size of the synthesized materials is calculated to be 12.47 nm using the Debye-Scherrer formula as given in equation 2.

$$\frac{1}{d^2} = \frac{h^2+k^2}{a^2} + \frac{l^2}{c^2} \tag{1}$$

$$D = \frac{k\lambda}{\beta \cos\theta} \tag{2}$$

where β represents the full width at half maximum of the XRD peak, λ is the X-ray wavelength (1.5406 Å), K is the Scherrer constant (numerical value equal to 0.93), and θ is the diffraction angle [33]. The X-ray density of a material will be found using the equation 3

$$\rho = \frac{nM}{NV} \tag{3}$$

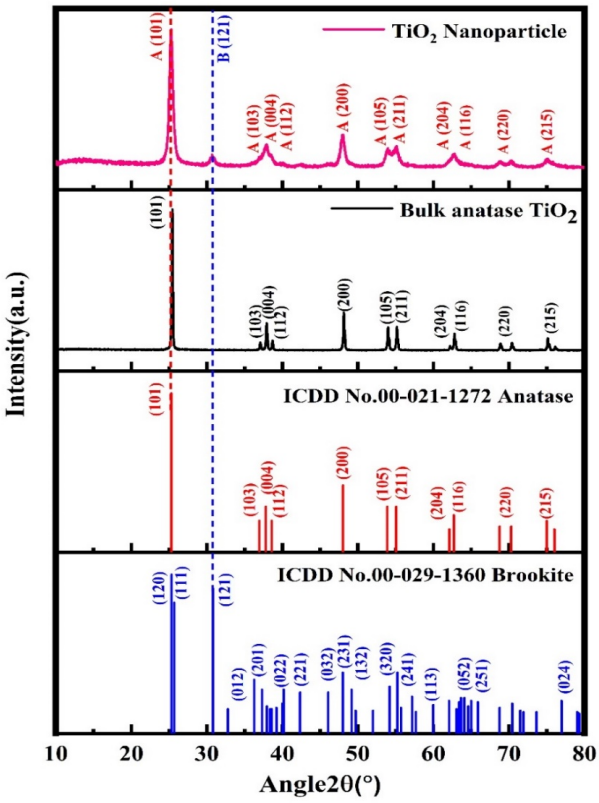

Figure 1. XRD pattern of TiO_2 nanoparticles.

where M corresponds to the molecular weight, N is the Avogadro number, and V is the unit cell volume (a2c); for the anatase phase, n is four. Further specific surface area is determined using the Sauter formulae 4.

$$\rho_D = \frac{6\times 10^3}{\rho^D} \tag{4}$$

Here, D is the crystallite size obtained from the Debye-Scherrer relation. The crystal contains crystallographic defects formed during the cell formation and is indicated in terms of a parameter known as dislocation density δ, which is the length of the dislocation lines per unit volume of the material [34, 35] and can be established using the following equation 5.

$$\delta = \frac{1}{D^2} \tag{5}$$

The phase compositions of nanoparticles can be calculated from the values of integral intensities of the XRD peaks of anatase (101) and brookite (121) using the Zhang and Banfield theory [36]. The crystal parameters which were obtained from XRD are shown in Table 1. The microstrain of the samples can be evaluated using Williamson and Hall plots. Williamson and Hall [37] proposed a Uniform deformation model (UDM) for obtaining the broadening due to crystal size and strain by taking the XRD peak width as a function of 2θ. In this model, the strain is supposed to have a common value in all crystallographic directions. In this model, the average crystallite size and strain can be related

Table 1. Summary of crystal parameters obtained from the XRD.

Calculated crystal parameters of TiO_2 nanoparticle	Annealing temperature (500 ^oC For 2h)	
Crystalline phases	**Anatase (101) plane**	**Brookite (121) plane**
Crystal structure	Tetragonal	Orthorhombic
Space group	$I_{41/amd}$	pbca
FWHM (Radian)	0.0113	0.0133
d-spacing ($\AA$)	3.5207	2.9070
Lattice parameters ($\AA$)	a=b=3.7884 c=9.5044	a=5.4558 b=9.1819 c=5.1429
Unit cell volume ($\AA^3$)	136.090	257.631
Crystallite Size D (nm)	12.473	10.747
Micro Strain,ε	0.00642	0.00865
Phase content fraction (wt %)	77.08	22.92
Dislocation density, δ	0.0127	0.0121
Specific Surface Area (m^2/g)	113.72	135.53

[38, 39] through the following equation 6,

$$\beta \cos\theta = \frac{K\lambda}{D} + 4\varepsilon \sin\theta \tag{6}$$

where β is the FWHM, θ is the angle of diffraction, K is the Scherrer constant, λ is the X-ray wavelength, D is the average particle size, and ε is the average strain. Here using $\beta\cos\theta$ along the X-axis and 4 $\sin\theta$ along the Y-axis, a graph can be drawn (W-H plot), linear fitting of which is done to obtain the average particle size as the Y-intercept, and the slope of the graph represents the value of strain. Theoretically speaking, compressive strain belongs to the negative slope value in the graph; the positive slope value indicates the occurrence of tensile strain, whereas the horizontal slope assures particle homogeneity free of microstrain [40, 41]. W-H plot for pure TiO_2 nanoparticles, shown in figure 2, gives the values of crystallite size and microstrain as 9.588 nm and 0.00197±0.00437, respectively. The positive slope indicates the presence of tensile strain and the gradual removal of grain boundary defects.

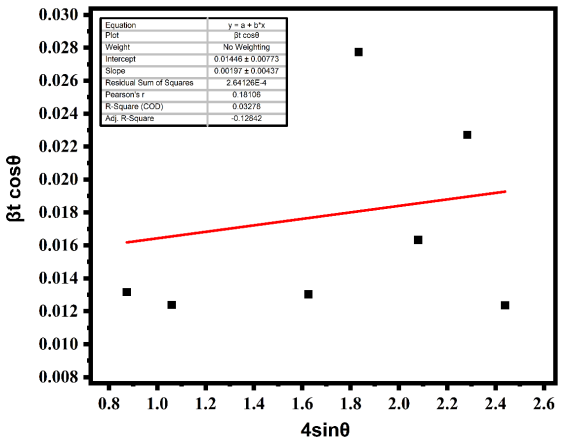

Figure 2. W-H plot for pure TiO_2 nanoparticles annealed at 500 ^oC for 2 hr.

3.2 Morphological studies

The homogeneity and uniform size distribution of the nanoparticles can be evaluated using FESEM images. The surface morphology of the TiO_2 nanoparticles obtained from the FESEM image is displayed in figure 3. We can observe homogenously distributed spherical-shaped nanoparticles having an average particle size of 17 nm. The average particle size obtained from FESEM differs only slightly from the XRD results. FESEM indicates a high degree of crystallinity to the TiO_2 nanoparticles, which is consistent with the result from XRD [42, 43].

The homogenous size distribution of the nanoparticles and their planes were confirmed through transmission electron spectroscopy. Figure 4 shows the (a) TEM, (b) HRTEM, and (c) SAED patterns of the mixed-phase nanoparticles. TEM shows homogenous crystalline particles with an average particle size in the range of 15nm, which matches the results of XRD and FESEM well. HRTEM shows the arrangement of atoms wherein the interplanar spacing is obtained to be 0.373 nm, which corresponds to the anatase TiO_2 (101) plane of the nanoparticles. Rings in the SAED pattern are indicative of anatase (101), (004), (200), (105), (211), (204), and brookite (121) planes in the nanoparticles.

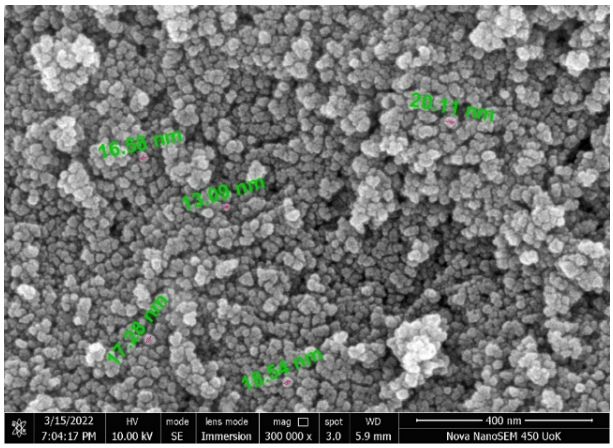

Figure 3. FESEM image of TiO_2 nanoparticles.

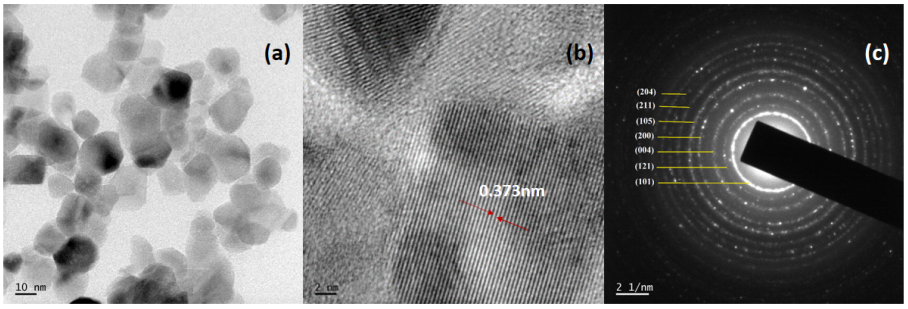

Figure 4. (a) TEM, (b) HRTEM, and (c) SAED pattern of the mixed-phase of TiO_2 nanoparticles.

3.3 Optical studies

The determination of the band gap is very significant for the optimization of the generation of electron/hole pairs in nanostructured semiconductor materials under illumination. The UV-visible spectra of the TiO_2 nanoparticles were recorded in order to calculate the band gap (E_g) of nanoparticles, which is compared with that of pure anatase TiO_2 in the bulk phase. The optical band gap can be calculated using the diffuse reflectance spectra employing the Kubelka Munk method [44]. The Kubelka – Munk function $F(R)$ and percentage reflectance R are related through the equation 7,

$$F(R) = \frac{(1-R)^2}{2R} \tag{7}$$

In this method, a graph is plotted with $(F(R)h\upsilon)^2$ along the Y-axis and energy $h\upsilon$ along the X-axis. The band gap of synthesized nanoparticles is determined by extrapolating the graph to the X-axis and taking the X intercept [45]. The UV-Vis spectrum and the Kubelka-Munk plot of the nanoparticles are shown in figure 5. The direct band gap of the nanoparticles is estimated as 3.265 eV which is found to be greater than the band gap of bulk TiO_2 (3.201 eV), indicating an increase in the band gap. The enhancement in the band gap of nanoparticles arises from the quantum confinement phenomena in nanoparticles, the presence of the brookite phase in the mixed phase nanoparticles also has a role in the increase of band gap.

3.4 Thermal studies

Post annealing of the nanoparticles helps in the removal of water and other impurities from the surface of nanoparticles. In order to validate the higher temperature stability of the nanoparticles and to fix the annealing temperature, TG analysis was performed. Figure 6 illustrates thermo gravimetric analysis of wet chemically synthesized TiO_2 nanoparticles. The TG-DTA studies shows a total loss of 9.3 wt% upon heating from room temperature to 800 °C. When the temperature is increased from room temperature to 100 °C, a weight loss of 2.46 wt% occurs. The reason for such a loss is the evaporation of solvent and the absorbed water. The loss of absorbed water from the Titania phase was supported by the appearance of an endothermic broad peak around (60 -150 °C) observed in differential thermal gravimetric analysis. A weight loss of 5.56 wt% occurs through a temperature range of 100 - 600 °C. A third weight loss of 1.28 wt% has taken place when the temperature is increased from 600 °C to 800 °C. The evaporation of the organic compound is the reason behind the second and third stages of weight loss. These results reveals that the synthesized TiO_2 nanoparticle possess thermal stability even at a higher temperature and annealing the sample at around 500

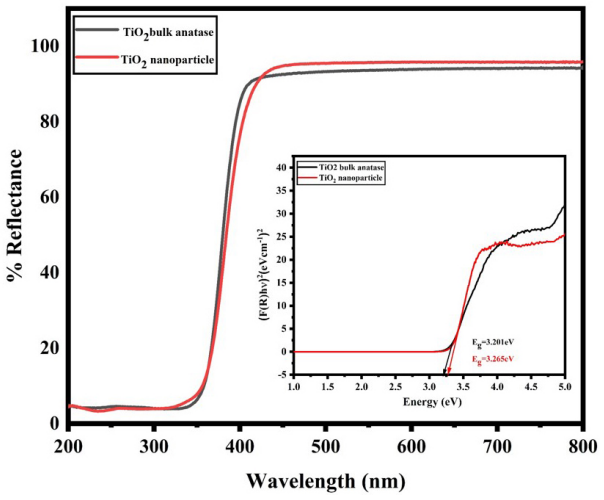

Figure 5. UV-visible reflection spectra of TiO_2 nanoparticles and bulk TiO_2 and band gap estimation using Kubelka-Munk plot.

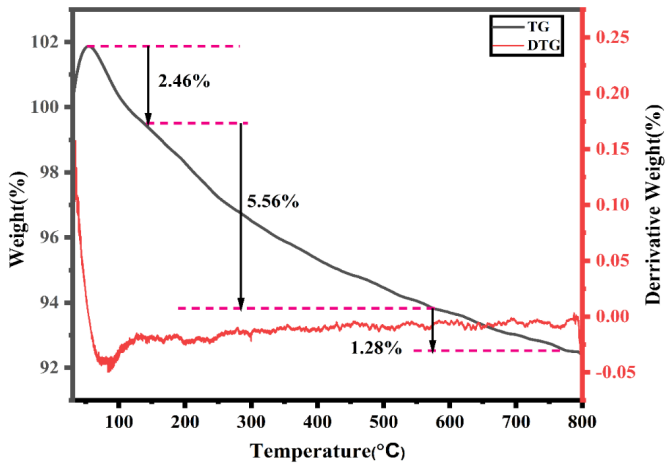

Figure 6. TG/DTA analysis of TiO_2 nanoparticles.

^{o}C just after the synthesis will help to eliminate majority of the impurities from our photocatalyst [46].

3.5 FTIR analysis

Vibrational studies of the nanoparticles were conducted using FTIR spectroscopy. Figure 7 displays the FTIR peaks of TiO_2 nanoparticles collected in the wavelength range 4000 - 400 cm^{-1}, which will enable us the determination of the vibrational bands and functional groups present in the synthesized samples. The region around 4000-1500 cm^{-1} corresponds to the stretching modes of functional groups, and the other region extended from 1500 cm^{-1} to 400 cm^{-1} stands for interatomic stretching and bending vibration modes of metal oxide absorption bands [47, 48]. The peak noticed at 405.95 cm^{-1} is due to the Ti-O stretching vibration mode. The peaks observed at 1640.28 cm^{-1} and 3351.02 cm^{-1} are characteristics of bending and stretching vibrational modes of O-H, which are associated with surface-adsorbed water. The broadband located at 3420 cm^{-1} corresponds to the brookite phase of TiO_2 [49].

3.6 EDX analysis

The EDX spectra of the synthesised sample shown in figure 8 displays the elemental analysis and chemical composition of the nanoparticles. The semi quantitative analysis of the sample shows atomic weight percentage values of 60.39% and of 39.61% for Ti and O respectively. The energy peaks around 4.5 KeV and 5 KeV represents Ti. The peaks at 0.5 KeV correspond to Ti and O and no other impurity peaks are observed. Thus, the EDX spectrum confirms the high purity of TiO_2 nanoparticles [50].

3.7 Photoluminescence studies

Figure 9 shows the photoluminescence emission spectra of the bulk and TiO_2 nanoparticles when excited at a wavelength of 320 nm. The peak positions remaining same, but the emission intensity got reduced in mixed phase nanoparticles compared to bulk anatase phase TiO_2 indicating lower probability of carrier recombination and extended recombination life time in the mixed phase. The intense PL emission

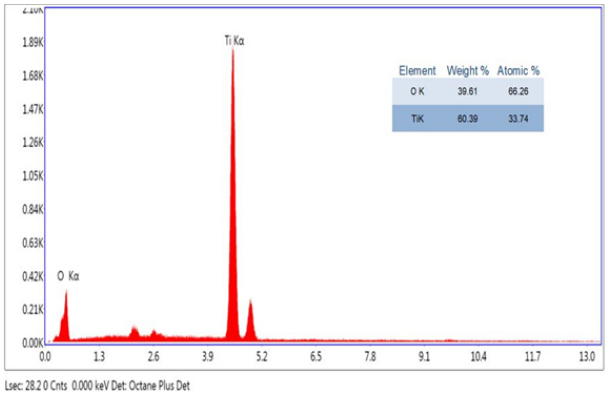

Figure 8. EDX spectra of synthesized TiO_2 nanoparticles (Inset shows the elemental percentage).

peak observed at 451 nm is due to the charge between Ti^{3+} and oxygen anion in the TiO_6^{8-} octahedral complex [51]. The oxygen vacancies or defects act as radiative centers, and it enhances the luminescence of TiO_2. The photoluminescence emission peak observed at 427 nm corresponds to the oxygen vacancies or defects. The emission band in the visible region (450-490 nm) is due to various intrinsic defects like Ti and O vacancies [52–54].

3.8 Raman studies

Raman spectrum of nanoparticles is depicted in figure 10, which is in agreement with the previous studies conducted by Ohsaka et al. [55]. According to their study, the unit cell of the Anatase phase has a bcc tetragonal structure having twelve atoms in a unit cell (space group I41/amd). Also, this phase occupies three infrared (IR) active modes (A_{2u} and $2E_u$), six Raman active modes ($A_{1g} + 2B_{1g} + 3E_g$), and a silent B_{2u} mode. The six allowed Raman modes of pure anatase phase of TiO_2 nanoparticles were observed in our Raman spectra at 141 cm^{-1} (E_g), 197 cm^{-1} (E_g), 395 cm^{-1} (B_{1g}), 519 cm^{-1} (A_{1g} or B_{1g}) and 638 cm^{-1} (E_g) [56, 57]. Among them, the sharp peak at 141 cm^{-1} (E_g) is due to the external vibrations of the anatase phase having long-range

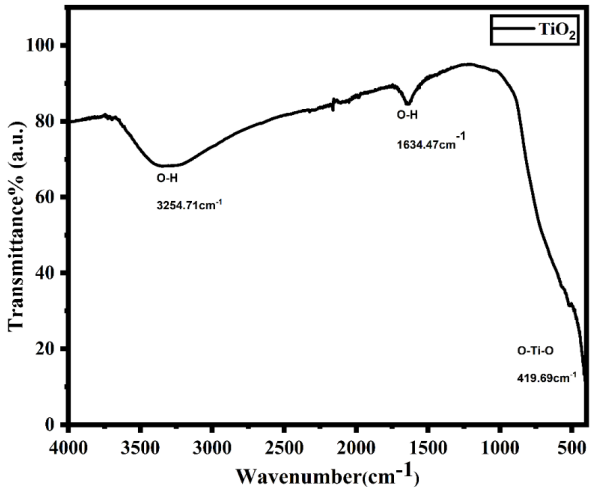

Figure 7. The FTIR spectrum of TiO_2 nanoparticles.

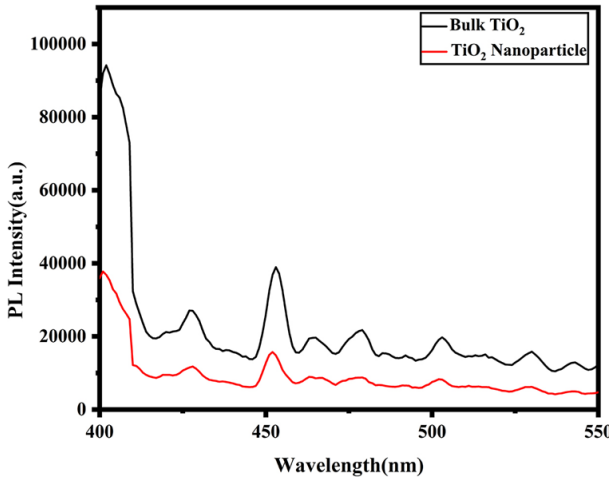

Figure 9. Photoluminescence emission spectra of the bulk and mixed-phase TiO_2 nanoparticles.

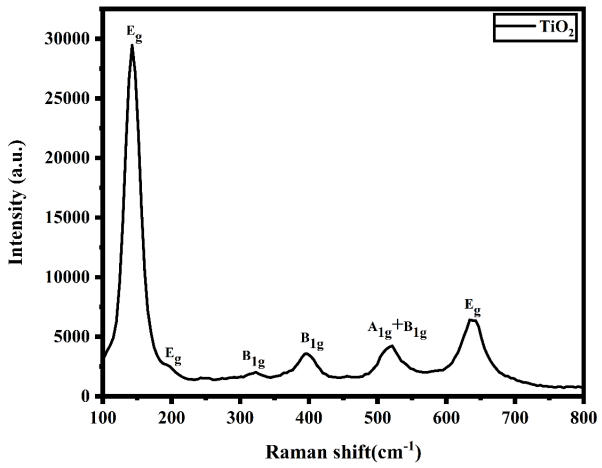

Figure 10. Raman spectra of synthesized mixed phase TiO_2 nanoparticles.

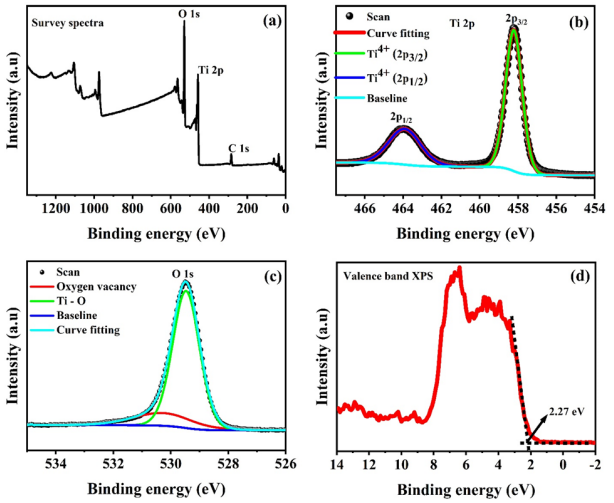

Figure 11. (a) XPS survey spectra of TiO_2 nanoparticles. XPS spectra of (b) Ti2p, (c) O1s, and (d) Valence band XPS spectra of TiO_2 nanoparticles.

order, whereas other weak peaks stand for short-range order vibrations of the anatase phase. The Raman studies also correlate the presence of the Brookite phase, with smaller peaks observed at 325 cm^{-1} (B_{1g}), 411 cm^{-1} (A_{1g}), 586 cm^{-1} (B_{2g}), and 638 cm^{-1} (A_{1g}), indicating the presence of brookite phase. The major Raman peak of the brookite phase at 150 cm^{-1} is not visible in our spectra; it might have merged with E_{1g} Raman mode at 141 cm^{-1}, thus affecting its width [58–60].

3.9 X-ray photoelectron spectroscopy studies

XPS analysis was conducted to determine the composition of the nanoparticles and identify the chemical states of the anatase and brookite phases. Figure 11 shows the XPS survey spectra of TiO_2 nanoparticles. The distinct peaks in the survey spectrum of Ti and O suggests the formation of the TiO_2 nanoparticles. Figure 11(b) and (c) shows the deconvoluted XPS spectra of spin-orbit signals of Ti2p and O1s. The Ti $2p_{3/2}$ peak at 458.24 eV and the Ti $2p_{1/2}$ peak at 464.07 eV confirm the presence of Ti^{4+} in the TiO_2 lattice [61]. The peak positions and peak separation value of 5.83 eV of the Ti2p doublet concur with the reported values for TiO_2 nanoparticles. The highest intense peak at 529.49 eV is assigned to the O1s, which is due to the lattice oxygen (Ti-O) in the anatase-brookite phase. A secondary peak appears at approximately 530.12 eV, which is indicative of oxygen vacancies that could influence the photocatalytic properties of the TiO_2nanoparticles. The characteristic signal C1s has a binding energy of 285.03 eV, and it is due to adsorbents of crystallite surface and grain boundaries. However, contaminations are inexorable for samples exposed to air. The absence of signals in the low-energy region confirms the purity and homogeneity of the synthesized nanoparticles [62]. The valence band edge positions of TiO_2 nanoparticles are determined using the VB-XPS, as shown in figure 11(d). The intersection of the fitted linear edge of the curve with the flat energy distribution in VB-XPS spectra gives the value of the valence band potential of the semiconductor (VVB), which is obtained to be 2.27 eV. Hence, the conduction band potential (VCB) was calculated to be -0.99 eV using the following relation 8 [63]

$$V_{CB} = V_{VB} - E_g \tag{8}$$

Table 2 shows atomic percentages of different elements obtained in the XPS spectra.

3.10 Photocatalytic studies

The mechanism of photocatalytic degradation by TiO_2 nanoparticles was described by Nasikhudin et al. [64] as well as Saqib et al. [65]. When TiO_2 nanoparticles are illuminated with a light energy value higher than the semiconductor band gap, the valence band electrons will move to reach the conduction band, thus leaving the holes behind in the valence band. The generated electron-hole pairs interact with the water and oxygen molecules or hydroxyl group, causing the production of reactive oxygen species such as superoxide anions ($*O_2^-$) and hydroxyl radicals (OH^*). These reactive oxygen species oxidise nearby water-soluble organic dye molecules, producing CO_2, H_2O, and other intermediates, ultimately resulting in their degradation. The role of free radicals on photocatalytic degradation can be established from the UV-Vis absorption spectrum as the scavengers will inhibit the dye degradation process [66]. The degradation of dye takes place via the formation of partially oxidized intermediates, which afterward undergo complete mineralization. Since the reactions predominantly

Table 2. Atomic percentages of elements obtained from X-ray photoemission spectrum.

Sample	Ti2p peak (eV)	O1s peak (eV)	C1s peak (eV)	Ti2p (at%)	O1s (at%)	C1s (at%)
TiO_2	458.24	529.49	285.03	20.68	49.55	29.77

occur on the surface of the nanoparticles, the concentration of dye molecules near the photocatalyst surface, surface adsorption of intermediate products, and recyclability of the photocatalyst have prime roles in improving the photocatalytic performance. The number of intermediates formed during the reduction of methylene blue using TiO_2 can be established through mass spectrometry analysis [67]. Here, we have employed the LC-MS-MS analysis to establish the type of intermediates formed during the dye degradation process after treatment with the photocatalyst [68]. To check the recyclability, the photocatalyst was separated from the dye solution through centrifugation after each degradation cycle and then washed with ethanol three times. After that, the powder was dried for 3 h at 80 ^{o}C in a hot air oven and used again for dye disintegration in the next cycle.

3.10.1 Mechanism of photocatalytic degradation by the TiO_2

The reactions involved in the degradation of the dye can be described as follows;

$$TiO_2 + h\upsilon(\text{Visible}) \rightarrow TiO_2(h^+ + e^-)$$

$$H_2O + h^+ \rightarrow OH^* + H^+$$

$$O_2 + e^- \rightarrow {}^*O_2^-$$

$$\text{Organic dye} + [{}^*O_2^- \text{ or } OH^*] \rightarrow \text{Degradation products}$$

In a typical photodegradation reaction, the kinetics of the reaction can well be interpreted by the Langmuir-Hinshelwood (L-H) model [69]. This model evaluates the adsorption extent of the incorporated dye (pollutant) and its degradation intermediates onto the catalyst's surface. Thus, the concentration of the dye and the photocatalyst play a vital role in this model. Monolayer adsorption of the adsorbed dye molecules at the solid-liquid interface is considered in the L-H model. Here, as the photocatalyst is in a heterogenous phase, the photocatalytic process obeys first-order kinetics, and the corresponding equations are,

$$C_t = C_0 e^{kt} \tag{9}$$

$$\ln\left(\frac{C_0}{C_t}\right) = kt \tag{10}$$

Here, C_0 and C_t represent the concentrations of dye molecules present initially and at a time t (in minutes), and k is the reaction rate of photocatalysis [70]. The UV absorbance of MB is directly related to its concentration obeying Beer Lambert's law given by equation 11,

$$A = \varepsilon c l \tag{11}$$

In the above equation, A is the optical absorbance of the sample, ε is the molar absorptivity constant, C is the concentration and l is the path length. If A_0 and A_t represent the absorbance of dye molecules present initially and after a time t (in minutes), then equation 10 leads to equation 12,

$$\ln\left(\frac{A_0}{A_t}\right) = kt \tag{12}$$

The percentage degradation efficiency of the photocatalyst is given by equation 13,

$$\text{Degradation efficiency}(\%) = \frac{(A_0 - A_t)}{A_0} \times 100 \tag{13}$$

In order to study the kinetics of the degradation processes, MB solutions were subjected to photodegradation experiments at different irradiation times. The absorbance of the MB solution was recorded using a UV–Vis spectrophotometer, and $\ln(A_0/A_t)$ was calculated using the Hinshelwood equation. For studying the kinetics of the photodegradation process, the calculated values of $\ln(A_0/A_t)$ were plotted as a graph against the degradation time. The slope of the Hinshelwood plot [$\ln(A_0/A_t)$ vs. time] gives the rate constant of the photodegradation process in the applied conditions [71].

3.10.2 Effect of photocatalyst loading and concentration of dye on photodegradation of methylene blue

Figure 12 shows the UV visible spectra of the untreated dye and dye upon treatment with bulk TiO_2 and nanoparticles at different loading amount (0.2 g/L, 0.4 g/L and 0.6 g/L). The variation of $\ln(A_0/A_t)$ and percentage of dye degradation with respect to time of bulk TiO_2 and nanoparticles on exposure to UV, Visible, and dark are shown in figure 13. The two absorption peaks observed at 664 nm and 605 nm, respectively, represent the absorption of MB monomer and dimer molecules.

The absorption spectra indicates that the absorbance of the MB decreases with the time after treating with the TiO_2 which is indicative of the degradation of methylene blue. It is observed that more than 60 % of dye molecules were dissociated within the first 120 minutes under UV as well as visible irradiation. It is interesting that the MB degradation rate by the photocatalyst is higher in the visible region than in the UV radiation (as observed from the sudden decrease in the absorption peak of MB with time). The TiO_2 nanoparticles exhibit minimum degradation in the dark mode. Here, in our results, the gradual reduction in the absorbance peak on exposure to UV as well as visible light indicates that the amount of oxidizable dye molecules decreases with the increase in time. The bulk TiO_2 is found to be more efficient in UV irradiation, whereas the nanoparticles show higher activity in visible irradiation.

The variation in the degradation efficiency of bulk and nanoparticles (different loading) are plotted as a function of time in figure 13(a), and the corresponding first-order kinetic potential plot is drawn in figure 13(b). The variation in the degradation efficiency of nanoparticles with increasing MB concentration for a fixed amount of the photocatalyst (0.2 g/L) is plotted in figure 13(c), and the corresponding first-order kinetic potential plot is shown in figure 13(d). The degradation efficiency of the photocatalyst increases from 61 to 81% (for 0.2 g/L photocatalyst), 85 to 90 % (for 0.4 g/L photocatalyst), and 82 to 95% (for 0.6 g/L photocatalyst) on exposure to visible light compared to UV light. The photodegradation rate constant is calculated by fitting a graph of $\ln(A_0/A_t)$ versus time with the linear equation of the first order kinetic potential model [72]; the slope of the straight line gives the rate constant. The percentage of degradation is also found to be increasing with the increase in the concentration (0.2 g/L to 0.6 g/L) of the photocatalyst in visible light (81 to 95%) exposure. Our results indicate that the majority of the dye molecules are

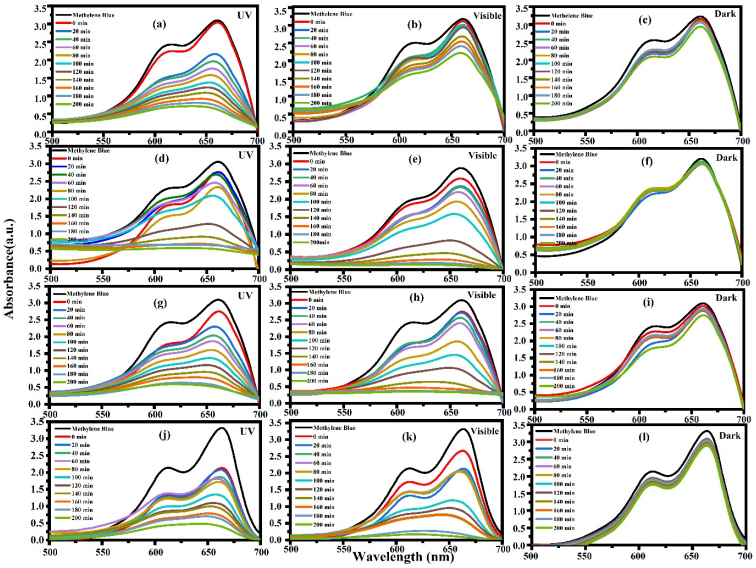

Figure 12. The UV-Vis spectrum of 0.05 mM MB solution treated with bulk TiO_2 (First row), 0.2 g/L (second row), 0.4 g/L (third row), and 0.6 g/L (fourth row) of TiO_2 nanoparticles collected at different time intervals upon irradiation with (a) UV light (b) sunlight (c) kept in the dark.

disintegrated within a short period of time (200 minutes) in both UV as well as visible irradiations, among which the visible exposure shows better activity. The calculated photo degradation rate constant for the bulk TiO_2, different loading of the photocatalyst, and different concentrations of dye under UV, visible, and dark conditions are listed in Table 3.

Here, the observed improvement in the rate constant with an increase in nanoparticle loading in the mixed phase also confirms enhancement in the degradation phenomena. This is based on the fact that higher amounts of TiO_2 provide more surface adsorption sites for the water molecules. As the concentration of TiO_2 increases, the adsorption sites on the surface will be increased, and it will enhance the number of photons absorbed on the photocatalyst surface, thereby decreasing the time for degradation of dye. It will lead to a higher generation of electron-hole pairs and a greater number of hydroxyl free radicals, thereby improving the number of adsorbed dye molecules on the photocatalytic surface, resulting in higher degradation efficiency [73]. It is found that

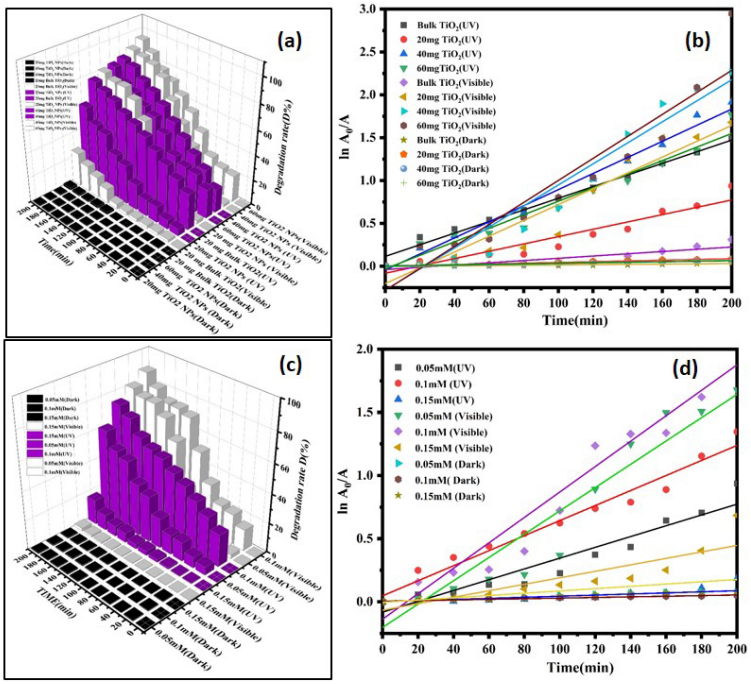

Figure 13. The upper row shows the (a) Variation in the degradation efficiency and (b) The first-order kinetic plot of bulk and different loading of TiO_2 nanoparticles treated with 0.05 mM methylene blue. The lower row indicates (c) Variation in the degradation efficiency and (f) An order kinetic plot of 0.2 g/L photocatalyst treated with different concentrations of MB.

Table 3. Variation of Photocatalytic rate constant of mixed-phase photocatalyst (keeping the different quantities of photocatalyst and dye) with respect to bulk anatase TiO_2.

Sample	Photocatalytic rate constant (min^{-1})		
	UV	Visible	Dark
Bulk TiO_2 (0.2 g/L) in MB(0.05 mM)	6.78×10^{-3}	1.32×10^{-3}	1.79×10^{-4}
TiO_{2NP} (0.2 g/L) in MB (0.05 mM)	4.46×10^{-3}	9.89×10^{-3}	1.79×10^{-3}
TiO_{2NP} (0.4 g/L) in MB (0.05 mM)	9.68×10^{-3}	14.11×10^{-3}	3×10^{-3}
TiO_{2NP} (0.6 g/L) in MB (0.05 mM)	7.9×10^{-3}	14.63×10^{-3}	2.85×10^{-4}
TiO_{2NP} (0.2 g/L) in MB (0.05 mM)	4.46×10^{-3}	9.89×10^{-3}	1.75×10^{-4}
TiO_{2NP} (0.2 g/L) in MB (0.1 mM)	5.95×10^{-3}	17.07×10^{-3}	2.45×10^{-4}
TiO_{2NP} (0.2 g/L) in MB (0.15 mM)	7.13×10^{-4}	2.56×10^{-3}	9.04×10^{-4}

the rate constant in the visible region increases sharply from 9.89×10^{-3} min^{-1} (for 0.05 mM) to 17.07×10^{-3} min^{-1} (for 0.1 mM) as the dye concentration changes and then found to decrease to 2.56×10^{-3} min^{-1} (for 0.15 mM) thereby showing a maximum value at an optimum concentration of 0.1 mM indicating a saturation of the dye degradation process at higher dye concentration. The sharp increase in the rate constant at 0.1 mM is in conformity with the highest photodegradation percentage observed at 0.1 mM concentration of dye in the visible region (Figure 14).

The improved photocatalytic activity (high-rate constant value) observed in the visible region by the mixed-phase nanoparticles indicates that more reaction sites in the photocatalyst are activated during visible light irradiation compared to UV irradiation. Thus, the obtained results indicate that the mixed-phase nanoparticles exhibit improved dye degradation compared to the performance of bulk anatase phase TiO_2. The high crystallinity and reduced particle size (increased surface area) of the TiO_2 in the nano-regime has a great role in improving the photocatalytic activity as it will enhance the number of pore (reaction sites) on the nanoparticle surface, which will effectively activate the solid-solid interactions. The presence of the brookite phase will have a strong influence on the high photocatalytic activity in the nanoparticles; the mixed phases of nanoparticles might cause a synergistic effect on the photocatalytic performance compared to that of pure anatase phase, and its mechanism is shown in figure 14(a). The image of the MB solution exposed to dark, UV, and visible irradiations after treatment with the bulk and mixed-phase photocatalyst after 200 minutes is shown in figure 15, which clearly indicates the effect of nanoparticles in the visible irradiation.

The improvement in the photocatalytic activity results from the junction effect between the two TiO_2 phases. The formation of the junction results from the shift in the conduction band edge of the brookite phase of TiO_2 more negatively relative to that of anatase [23, 27]. This leads to the generation of type II band alignment (staggered gap) in the junction structure assigned by variations in the conduction band of both phases that will effectively facilitate maximum charge separation and the interfacial transfer of electrons from the brookite phase to the anatase phase. This happens because the relative positions of the valence and conduction bands in the staggered type permit the movement of electrons from the conduction band of the brookite phase to that of the anatase phase, whereas the holes are moved from the valence band of anatase to that of brookite [74–76]. The energy barrier separation will prevent the back-electron transfer, which will decrease the possibility of electron-hole recombination. The photogenerated holes transferred to the surface react with the hydroxide anions and water molecules present on the surface of TiO_2 nanoparticles, pro-

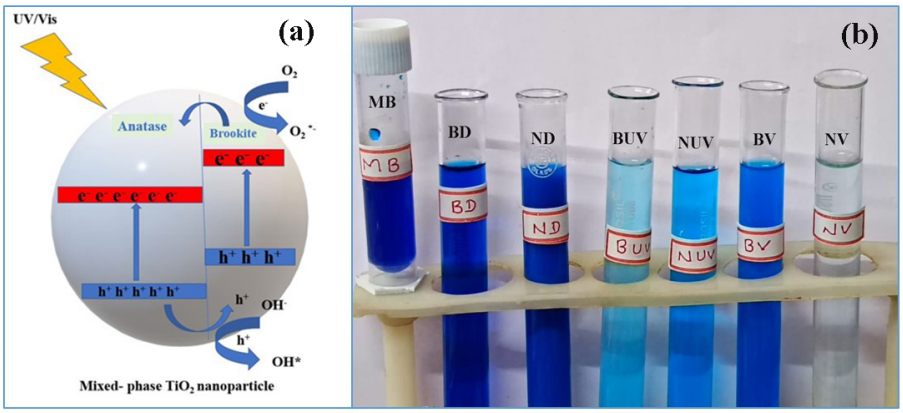

Figure 14. (a) Proposed mechanism demonstrating electron transfer in anatase-brookite photocatalyst (b) Degradation of methylene blue solution under UV-Vis. irradiation (MB. Untreated, BD. Treated with bulk TiO_2 in the dark, ND. Nano TiO_2 in the dark, BUV. Bulk TiO2 in the UV, NUV. Nano TiO_2 in the UV, BV. Bulk TiO_2 in the visible, NV. Nano TiO_2 in the visible).

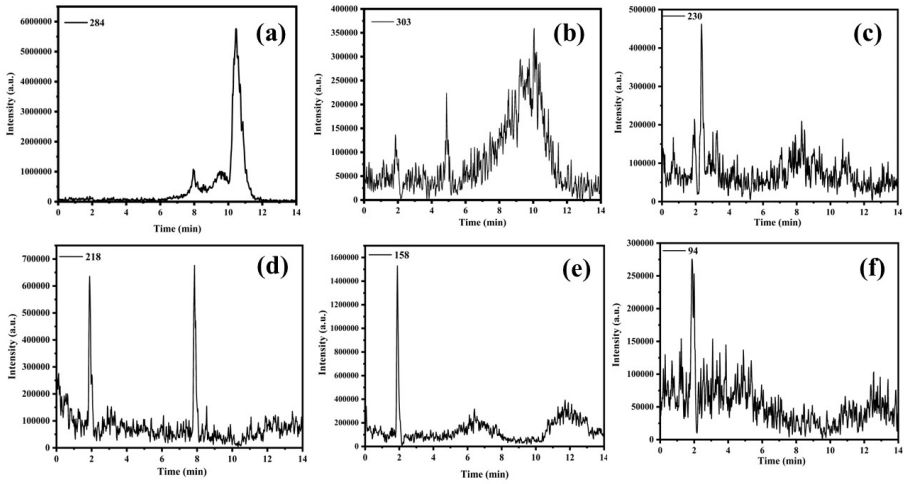

Figure 15. MS chromatograms of (a) MB with m/z ratio of 284 (b) reaction intermediate with m/z ratio of 303 (c) reaction intermediate with m/z ratio of 230 (d) reaction intermediate with m/z ratio of 218 (e) reaction intermediate with m/z ratio of 158 (f) reaction intermediate with m/z ratio of 94. The X-axis stands for retention time, and the Y-axis stands for signal intensity.

ducing strongly reactive OH* radicals with strong oxidative capability [77]. Also, superoxide anion radicals will be generated due to the reaction of photogenerated electrons on the adsorbed oxygen molecules [78, 79]. Both species thus causes the oxidative degradation of dye molecules into H_2O and CO_2. Thus, the improved photocatalytic performance owes to the more beneficial charge transfer between the anatase-brookite phases in the biphasic system. The reduced particle size and increased surface area of the brookite phase also help in facilitating the efficient transport and diffusion of methylene blue molecules to the active sites within the mixed-phase of TiO_2 nanoparticles. Also, this improvement in activity is partially ascribed to the higher crystallinity of brookite, as crystallinity is a more important factor than surface area in the mechanism of photocatalysis [80]. At the same time, it is true that the improved photocatalytic activity results from a combination of factors inherent to the prepared photocatalysts; it is crucial to evaluate the significance of the brookite phase in enhancing this activity in the visible region. Also, the contribution from the phenomenon of photosensitization in the dye leading to the electron injection from photoexcited dye molecules to photocatalysts also has to be considered. Therefore, it is imperative to conduct an in-depth experimental analysis in the future to allocate more focused attention to these aspects and, hence, to validate whether there exists any selective mechanism behind the brookite phase's contribution to the high photocatalytic activity in the visible region.

3.10.3 Analysis of the intermediate products through LC-MS-MS analysis

Methylene blue (MB) undergoes photocatalytic degradation upon treatment with TiO_2 nanoparticles, producing different fragmented compounds, which was confirmed by their mass spectra signals using LC-MS-MS analysis [81]. The mass spectrometry (MS) chromatograms of different intermediates are shown in figure 15, which indicates degradation of the chromophoric group as reported by Yang et al. [82]. In the degradation pathway of chromophoric group, initially the hydroxyl radical reacts with the MB and cleave their C-N=C bond led to the formation of sulfoxide compound (m/z 303). This sulfoxide compound is further converted in steps to 2-amino-5-(N-methyl formamide) benzene sulfonic acid (m/z 230), 2-amino-5- (methyl amino) –hydroxy benzene sulfonic acid (m/z 218), benzenesulfonic acid (m/z 158) and finally to phenol (m/z 94).

3.10.4 Effect of pH, scavengers, and reusability of the photocatalyst

The variation in the degradation percentage for 0.05 mM MB dye treated with 0.2 g/L of photocatalyst upon adding different scavengers (taken at t=120 minutes) is shown in figure 16(a). It is observed that the presence of the scavengers inhibits the degradation process, as indicated by the reduction in the percentage of degradation, confirming the role of active species in improving the degradation process [66]. The initial pH of the solution is one of the most important parameters in photocatalytic degradation processes as it influences the electrical charge characteristics and ionization state of the catalyst surface [83]. The variation in the percentage of degradation of MB dye (0.05 mM) by 0.2 g/L photocatalyst with varying pH is shown in figure 16(b). It is observed that the photocatalyst showed the least performance at pH 3 (acidic medium) and the highest performance at pH 11 (basic medium). The interpretation of pH effects on the photocatalytic process is very difficult to interpret due to its multiple roles, such as electrostatic interactions among the photocatalyst surface, solvent, dye molecules, and charged radicals species produced during the degradation process. Here, the increase in the degradation of basic pH is due to the following facts, as reported by Nasikhudin et al. [64]. In the neutral condition, the hydroxyl radical ($OH^{\star}$) is produced when a hole interacts with the water molecule to produce H^+ and $OH^{\star}$. In the basic pH, the hy-

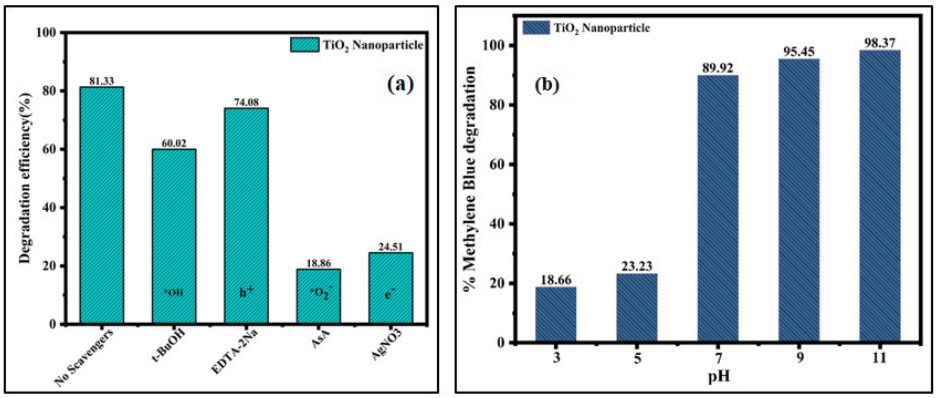

Figure 16. (a) Effect of scavengers of active species on the percentage of photocatalytic degradation taken after 120 minutes (0.2 g/L mg photocatalyst and 0.05 mM dye) (b) The percentage degradation of MB dye (0.05 mM) by 0.2 g/L photocatalyst with variation in the pH.

droxyl radical OH* will be generated directly from the OH- ion due to its reaction with a hole. Hence the quantity of hydroxyl radical will be more compared to neutral solutions that its photocatalytic performance will be better. The pH value has a strong influence on the dissociation capacity of materials, the charge distribution on the catalyst surface, and the oxidation potential of the valence band of the catalyst. In acidic conditions, there exists an excess of H+ so that this excess H+ will interact with the electrons to form radicals (H*) which will interact with OH* and produce water again. This results in the reduction of a number of OH* radicals, leading to lesser photocatalytic activity under acidic conditions. Also, the reusability of the photocatalyst is confirmed [84] by using the same photocatalyst powder (0.2 g/L) for five cycles, and the degradation efficiency shown in figure 17 indicates that the photocatalytic efficiency of the photocatalyst does not suffer much depreciation after each use indicating the stability of the photocatalytic system.

Thus, we have conducted an in-depth study on the photocatalytic phenomena using mixed phase TiO_2 nanoparticles and the influence of a number of parameters on the photocatalytic performance such as quantity of photocatalyst and dye, influence of pH and free radicals and recyclability of photocatalyst. The study proposes that future research directions must provide deep insights into the phenomenon behind the enhancement in the photocatalytic activity in the visible region and fabrication of novel visible-light-driven non-toxic photocatalytic materials offering low-cost environmental remediation.

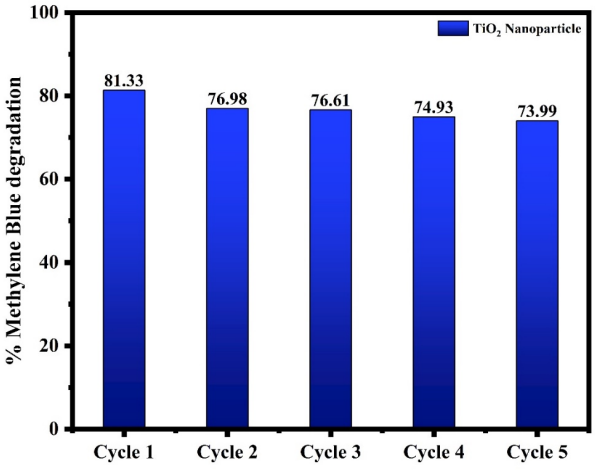

Figure 17. The percentage degradation of MB dye by the photocatalyst after different cycles of usage.

4. Conclusions

In conclusion, anatase–brookite mixed phase TiO_2 nanoparticles with high crystallinity were prepared by a simple, cost-effective route. The structural, compositional, thermal, and optical properties of mixed-phase TiO_2 nanoparticles were evaluated using a variety of characterization techniques. The photocatalytic properties of the nanoparticles were examined through the degradation of methylene blue under dark, UV, and visible irradiation. The improved photocatalytic efficiency of the nanoparticles can be attributed to a synergistic effect between the anatase and brookite TiO_2 phases. The formation of a bi-phase junction structure in the mixed phase creates a difference in the band gap, which in turn increases the separation efficiency of photoelectrons and holes, resulting in the improvement of the photocatalytic performance. The supportive effect from the crystallinity, as well as increased surface area owing to the nanosize regime, also have contributed to the high activity. The generation of the free radicals and their impact on photocatalysis are validated using the scavenger method. The study established that the photocatalytic performance is maximum in the basic pH conditions. The recyclability of the nanoparticles was established even after five cycles. The LC-MS-MS analysis established the reaction pathway and presence of intermediates during the dye degradation process. The high photocatalytic performance of the mixed-phase TiO_2 nanoparticles will enable its minimal use as a potential photocatalyst in the visible region for the low-cost environmental remediation purpose in an industrial perspective in comparison with its bulk single-phase counterpart.

Acknowledgement
MS Monisha acknowledges the University of Kerala for the research fellowship. The authors are grateful to CLIF- the University of Kerala, SAIF- M G University, and IISER-Thiruvananthapuram for providing characterization facilities. The authors thank the Department of Biotechnology, University of Kerala, for providing a UV-visible spectrophotometer facility for photocatalytic studies, the Department of Optoelectronics for providing the FESEM facility, and the Department of Physics, Alagappa University, for providing the Raman Spectra analysis facility.

Supplementary information
Catalyst characterization and UV-Vis profiles are available in supplementary.

Authors Contributions
Authors were equally contributed in acquisition and analysing the data as well as preparing the paper.

Availability of Data and Materials
Data is available on request from the corresponding author, upon reasonable request.

Conflict of Interests
The authors declare that they have no known competing financial interests or personal relationships that could have appeared to influence the work reported in this paper.

References

[1] M. F. Hanafi and N. Sapawe. *Mater. Today.*, **31**(2020):A141–A150, . DOI: https://doi.org/10.1016/j.matpr.2021.01.258.

[2] M. Malhotra, K. Poonia, P. Singh, A. A. P. Khan, P. Thakur, and P. Raizada. *J. Taiwan Inst. Chem. Eng.*, **158**(2024):1876–1070. DOI: https://doi.org/10.1016/j.jtice.2023.104945.

[3] A. Yousefi and A. Nezamzadeh-Ejhieh. *Iran. J. catal.*, **11**(2021)(3):247–259. DOI: https://doi.org/10.1021/acs.oprd.7b00354.

[4] G. M. Meselhy, M. Y. Nassar, I. M. Nassar, and S. H. Seda. *Materials Research Innovations*, **108** (2024):1–9. DOI: https://doi.org/10.1080/14328917.2024.2304927.

[5] H. Yousef. **8**(2023)(6):49–60. DOI: https://doi.org/10.21608/BJAS.2023.215490.1182.

[6] M. Y. Nassar, E. I. Alia, and E. S. Zakaria. *RSC Adv.*, **7**(2017):8034–8050. DOI: https://doi.org/10.1016/j.jhazmat.2010.01.095.

[7] M. Andrade-Guel, L. Diaz-Jimenez, and D. Cortes-Hernandez. *Bol. Soc. Esp. Ceram. Vidr.*, **58**(2018)(4):171–177. DOI: https://doi.org/10.1016/j.bsecv.2018.10.005.

[8] A. M. Alotaibi, S Sathasivam, B. A. D. Williamson, A. Kafizas, C. Sotelo-Vazquez, A. Taylor, D. O. Scanlon, and I. P. Parkin. *Chem. Mater.*, **30**(2018)(4):1353–1361. DOI: https://doi.org/0.1021/acs.chemmater.7b04944.

[9] M. Honda, T. O. P. Listiani, Y. Yamaguchi, and Y. Ichikawa. *Materials*, **16**(2023)(2):639. DOI: https://doi.org/10.3390/ma16020639.

[10] R. Desai, S. K. Gupta, S. Mishra, P. K. Jha, and A. Pratap. *Int. J. Nanosci*, **10**(2011)(6):1249–1256, . DOI: https://doi.org/10.1142/S0219581X11008381.

[11] M. A. Behnajady, H. Eskandarloo, N. Modirshahla, and M. Shokri. *Desalination.*, **278**(2011):10–17. DOI: https://doi.org/10.1016/j.desal.2011.04.019.

[12] D. K. Muthee and B. F. Dejene. *Heliyon.*, **7**(2021): 846–849. DOI: https://doi.org/10.1016/j.heliyon.2021.e07269.

[13] A. Purabgola, N. Mayilswamy, and B. Kandasubramanian. *Environ Sci Pollut Res*, **29**(2022):32305–32325. DOI: https://doi.org/10.1007/s11356-022-18983-9.

[14] P. Dhull, A. Sudhaik, V. Sharma, P. Raizada, V. Hasija, N. Gupta, T. Ahamad, V. H. Nguyen, A. Kim, M. Shokouhimehr, and S. Y. Kim. *Mol. Catal.*, **539**(2023):2468–8231. DOI: https://doi.org/10.1016/j.mcat.2023.113013.

[15] A. Bembibre, M. Benamara, M. Hjiri, E. Gomez, H. R. Alamri, R. Dhahri, and A. Serra. *J. Chem. Eng.*, **427**(2006)(13):1385–8947. DOI: https://doi.org/10.1016/j.cej.2021.132006.

[16] D. R. Eddy, M. D. Permana, L. K. Sakti, G. A. N. Solihudin, S. Hidayat, T. Takei, N. Kumada, and I. Rahayu. *Nanomaterials.*, **13**(2023)(4):1385–8947. DOI: https://doi.org/10.3390/nano13040704.

[17] G. Nagaraj, R. A. Senthil, and K. Ravichandran. *Mater. Res. Express.*, **6095049**(2019):9281–9282. DOI: https://doi.org/10.1088/2053-1591/ab2eec.

[18] T. Tio. *Chem. Rev.*, (2014):9281–9282. DOI: https://doi.org/10.1021/cr500422r.

[19] L. A. Kolahalam, I. V. Kasi Viswanath, B. S. Diwakar, B. Govindh, V. Reddy, and Y. L. N. Murthy. *Mater. Today Proc.*, **18**(2019):2182–2190. DOI: https://doi.org/10.1016/j.matpr.2019.07.371.

[20] M. T. Noman, A. M. Ashraf, and A. Ali. *Environ. Sci. Pollut. Res.*, **26** (2019)(4):3262–3291. DOI: https://doi.org/10.4028/www.scientific.net/NHC.19.46.

[21] M. A. Irshad. *Ecotoxicol. Environ. Saf.*, **212**(2021):105399. DOI: https://doi.org/10.1016/j.ecoenv.2021.111978.

[22] T. Luttrell, S. Halpegamage, and Tao J. *Sci Rep*, **4043**(2014). DOI: https://doi.org/10.1038/srep04043.

[23] P. Szoldra, M. Frac, R. Lach, L. Zych, M. Radecka, A. Trenczek-Zajac, and W. Pichor. *Mater. Sci. Eng. B.*, **287**(2024). DOI: https://doi.org/10.1016/j.mseb.2022.116104.

[24] A. A. Ismail, T. A. Kandiel, and D. W. Bahnemann. *J. Photochem. Photobiol. A Chem.*, **216**(2010):183–193. DOI: https://doi.org/10.1016/j.jphotochem.2010.05.016.

[25] J. C. Yu, J. Yu, W. Ho, and L. Zhang. *Chem. Commun.*, (2001). DOI: https://doi.org/10.1039/B105471F.

[26] O. Toshiaki, M. Iwasaki, H. Tada, T. Akita, K. Tanaka, and S. Ito. *J. Colloid Interface Sci.*, **281**(2005)(2):510–13. DOI: https://doi.org/10.1016/j.jcis.2004.08.137.

[27] A. D. Paola, M. Bellardita, and L. Palmisano. *Catalysts*, **3** (2013):36–73. DOI: https://doi.org/10.3390/catal3010036.

[28] P. O. Oladoye, T. O. Ajiboye, E. O. Omotola, and O. J. Oyewola. *Results Eng.*, (2022):2590–1230. DOI: https://doi.org/10.1016/j.rineng.2022.100678.

[29] W. Nachit, S . Touhtouh, Z. Ramzi, M. Zbair, A. Eddiai, M. Rguiti, and A. Bouchikhi. *ICFPAM*, **627**(2015). DOI: https://doi.org/10.1080/15421406.2015.1137135.

[30] M. A. Khan, M. S. Akhtar, and O. B. Yang. *Sol. Energy.*, **84**(2010):2195–2201. DOI: https://doi.org/10.1016/j.solener.2010.08.008.

[31] J. J. Park, D. Y. Kim, J. G. Lee, Y. H. Cha, M. T. Swihart, and S. S. Yoon. *RSC Advances*, **4**(2014:8661–8670, . DOI: https://doi.org/10.1039/C3RA47998F.

[32] A. K. Tripathi, M. K. Singh, M. C. Mathpal, S. K. Mishra, and A. Agarwal. *J. Alloys Compd.*, **549**(2013):114–120. DOI: https://doi.org/10.1016/j.jallcom.2012.09.012.

[33] A. L. Patterson. *Phys. Rev.*, **56**(1939):978–982. DOI: https://doi.org/10.1103/PhysRev.56.978.

[34] P. Bindu and S. Thomas. *J Theor Appl Phys*, **8**(2014): 123–134. DOI: https://doi.org/10.1007/s40094-014-0141-9.

[35] M. Saleem, L. Fang, H. B. Ruan, F. Wu, Q. L. Huang, C. L. Xu, and C. Y. Kong. *Intl. J. Phy. Sci.*, **7**(2012)(23):2971–2979. DOI: https://doi.org/10.5897/IJPS12.219.

[36] H. Zhang and J. F. Banfield. *J. Phys. Chem. B*, **104**(2000):3481–3487. DOI: https://doi.org/10.1021/jp000499j.

[37] G. K. Williamson and W. H. Hall. *Acta Metall*, **1**(1953):22–31. DOI: https://doi.org/10.1016/0001-6160(53)90006-6.

[38] V. D. Mote, Y. Purushotham, and B. N. Dole. *J. Theor. Appl. Phys.*, **6**(2012)(6). DOI: https://doi.org/10.1186/2251-7235-6-6.

[39] G. Rajender and P. K. Giri. *J. Alloys Compd.*, **676**(2016):591–600. DOI: https://doi.org/10.1016/j.jallcom.2016.03.154.

[40] A. Maurya, P. Chauhan, S. K. Mishra, and R. K. Srivastava. *J. Alloys Compd.*, **509**(2011):8433– 8440. DOI: https://doi.org/10.1016/j.jallcom.2011.05.108.

[41] B. Choudhury and A. Choudhury. *Int. Nano Lett.*, **3** (2013):3–55. DOI: https://doi.org/10.1186/2228-5326-3-55.

[42] M.K. Hossain, M.F. Pervez, M.N.H. Mia, S. Tayyaba, M.J. Uddin, and R. Ahamed. *Mater. Sci.*, **35**(2017): 868–877. DOI: https://doi.org/10.1515/msp-2017-0082.

[43] A. Sharma, Karn, and S. K. Pandiyan. *J Basic Appl Eng Res*, **1**(2014):1–5. DOI: https://doi.org/10.1016/j.matpr.2021.03.207.

[44] P. Kubelka. *Josa.*, **38**(1948)(5):448–457. DOI: https://doi.org/10.1364/JOSA.38.000448.

[45] B. D. Viezbicke, S. Patel, B. E. Davis, and D. P. Birnie III. *Physica status solidi (b)*, **252**(2015)(8):1700–1710. DOI: https://doi.org/10.1002/pssb.201552007.

[46] A. Kubiak, K. Siwinska-Ciesielczyk, and Z. Bielan. *Adsorption*, **25**(2019):309–325. DOI: https://doi.org/10.1007/s10450-019-00011-x.

[47] J. Coates, R.A. Meyers, and M.L. McKelvy. *EAC. 12 John Wiley & Sons Ltd. Chichester*, (2000):10815–10837. DOI: https://doi.org/10.1002/9780470027318.a5606.

[48] E. E. Ahmed, M. A.and El-Katori and Z. H. Gharni. *J. Alloys Compd.*, **553**(2013):19–29. DOI: https://doi.org/10.1016/j.jallcom.2012.10.038.

[49] M. Ruidiaz-Martinez, M. A. Alvarez, M. V. LOpez-RamOn, G. Cruz-Quesada, J. Rivera-Utrilla, and M. Sanchez-Polo. *Catalysts*, **520**(2020)(10). DOI: https://doi.org/10.3390/catal10050520.

[50] M. M. Ba-Abbad, A. A. Kadhum, B. M. S. Mohamad, H. A.and Takriff, and K. Sopian. *Int. J. Electrochem. Sci.*, **7**(2012):4871– 4888. DOI: https://doi.org/10.1016/S1452-3981(23)19588-5.

[51] V. K. S. Rhatigan, S. Mathew, M. C. Michel, J. Bartlett, M. Nolan, S. J. Hinder, A. Gasco, C. Ruiz-Palomar, and D. Hermosilla. *JPhys Materials*, **3**(2020)(2). DOI: https://doi.org/10.1088/2515-7639/ab749c.

[52] C. C. Mercado, F. J. Knorr, J. L. McHale, S. M. Usmani, A. S. Ichimura, and L. V. Saraf. *J. Phys. Chem. C.*, **116**(2012):10796–10804. DOI: https://doi.org/10.1021/jp301680d.

[53] M. S. F. A. Zamri and N. Sapawe. *Mater. Today: Proc.*, **19**(2019):1321–1326. DOI: https://doi.org/10.1016/j.matpr.2019.11.144.

[54] K. Vanheusden, W. L. Warren, C. H. Seager, D. R. Tallant, J. A. Voigt, and B. E. Gnade. *J. Appl. Phys.*, **79**(1996):7983–7990. DOI: https://doi.org/10.1063/1.362349.

[55] T. Ohsaka. *J. Phys. Soc. Jpn.*, **48**(1980):1661–1668. DOI: https://doi.org/10.1143/JPSJ.48.1661.

[56] C. A Chen, A. Korotcov, Ying-Sheng Huang, W. H. Chung, D. S. Tsai, and K. K. Tiong. *J. Mater. Sci.: Mater. Electron.*, **20**(2009):332–335, . DOI: https://doi.org/10.1007/s10854-008-9611-7.

[57] C. A. Chen, Y.S. Huang, and W.H. Chung. *J. Mater. Sci.: Mater. Electron.*, **20**(2009):303–306, . DOI: https://doi.org/10.1007/s10854-008-9595-3.

[58] M. Rezaee, S Mohammad, M. Khoie, and K. H. Liub. *Cryst Eng Comm*, **13**(2011)(16):5055–5061. DOI: https://doi.org/10.1039/C1CE05185G.

[59] R. Desai, S. K. Gupta, S. Mishra, P. K. Jha, and A. Pratap. *Int. J. Nanosci.*, **10**(2011)(6):1249–1256, . DOI: https://doi.org/10.1142/S0219581X11008381.

[60] S. Gayathri, M. Kottaisamy, and V. Ramakrishnan. *AIP Adv.*, **5**(2015):127219. DOI: https://doi.org/10.1063/1.4938544.

[61] W. Xie, R. Li, and Q. Xu. *Sci. Rep.*, **8**(2018):8752. DOI: https://doi.org/10.1038/s41598-018-27135-4.

[62] T. Park, W. C. Back, S. S. Mitchel, S. Kim, J. Elhamri, S. B. Boeckl, R. Fairchild, R. Naik, and A. A. Voevodin. *Sci. Rep*, **5**(2015):14374, . DOI: https://doi.org/10.1038/srep14374.

[63] K. Song, J. Gou, L. Yang, and C. Zeng. *Catal Lett*, **153**(2023):534–543. DOI: https://doi.org/10.1007/s10562-022-03997-2.

[64] N. Nasikhudin, M. Diantoro, A. Kusumaatmaja, and K. Triyana. *IOP Conf. Series: JPCS*, **1011**(2018): 012069. DOI: https://doi.org/10.1088/1742-6596/1011/1/012069.

[65] N. U. Saqib, R. Adnan, and I. Shah. *Environ. Sci. Pollut. Res.*, **23**(2016)(23):15941–15951. DOI: https://doi.org/10.1007/s11356-016-6984-7.

[66] A. Trenczek-Zajac, M. Synowiec, K. Zakrzewska, K. Zazakowny, K. Kowalski, A. Dziedzic, and M. Radecka. *ACS Appl. Mater. Interfaces.*, **14**(2022)(33):38255–38269. DOI: https://doi.org/10.1021/acsami.2c06404.

[67] M. V. D. Liz, R. M. D. Lima, B. D. Amaral, B. A. Marinho, J. T. Schneider, N. Nagata, and P. Peralta-Zamora. *J. Braz. Chem. Soc.*, **29**(2017)(2):380–389. DOI: https://doi.org/10.21577/0103-5053.20170151.

[68] M. K. Kesir and Z. Biyiklioglu. *Journal of Organometallic Chemistry*, **1005**(2024):122969. DOI: https://doi.org/10.1016/j.jorganchem.2023.122969.

[69] H. D. Tran, D. Q. Nguyen, P. T. Do, and U. N. P. Tran. *RSC Adv*, **13**(2023):16915–16925. DOI: https://doi.org/10.1039/D3RA01970E.

[70] S. Singh, G. K. Sidhu, and H. Singh. *Indian Chem. Eng.*, **61** (2019):28–39. DOI: https://doi.org/10.1080/00194506.2017.1408431.

[71] D. Hai Tran, D. Dinh Quan Nguyen, T. Phuong, T. N. P. Do, and T. Tran Uyen. *RSC Adv*, **13**(2023):16915–16925. DOI: https://doi.org/10.1039/D3RA01970E.

[72] S. A. Mirsalari and A. Nezamzadeh-Ejhieh. *Mater. Sci. Semicond. Process.*, **122**(2021):105455. DOI: https://doi.org/10.1016/j.mssp.2020.105455.

[73] Z. Wang, Y. Song, X. Cai, J. Zhang, T. Tang, S. Wen, and R. Soc. *Open Sci.*, **6**(2019)(10):191077. DOI: https://doi.org/10.1098/rsos.191077.

[74] T. A. Kandiel, L. Robben, A. Alkaima, and D. Bahnemann. *Photochem. Photobiol. Sci.*, **12**(2013):602–609. DOI: https://doi.org/10.1039/c2pp25217a.

[75] A. Kumar, M. Khan, J. He, and I. M.C. Lo. *Water Res.*, **170**(2020):115356. DOI: https://doi.org/10.1016/j.watres.2019.115356.

[76] O. A. Arotiba, B. O. Orimolade, and A. Koiki. Babatunde. *Curr. Opin. Electrochem.*, **22**(2020):25–34. DOI: https://doi.org/10.1016/j.coelec.2020.03.018.

[77] J. W. Ha, T. P. A. Ruberu, R. Han, B. Dong, J. Vela, and N. Fang. *J. Am. Chem. Soc*, **136**(2014)(4): 1398–1408. DOI: https://doi.org/10.1021/ja409011y.

[78] L. Zhu, A. S. Poyraz, C. H. Kuo, R. Miao, Y. Meng, and S. Y. Chen. *Chem. Mater.*, **27**(2015)(1):6–17. DOI: https://doi.org/10.1021/cm5035112.

[79] C. Konstantina, F. Guo, S. Elouatik, and G. P. Demopoulos. *Catalysts*, **10**(2020)(4):407. DOI: https://doi.org/10.3390/catal10040407.

[80] S. Vaclav and K. Daniela. *Mater. Chem. Phys*, **129**(2011):794–801. DOI: https://doi.org/10.1016/j.matchemphys.2011.05.006.

[81] P. Bansal, D. Singh, and D. Sud. *Sep. Purif. Technol.*, **72**(2010)(3):357–365. DOI: https://doi.org/10.1016/j.seppur.2010.03.005.

[82] C. Yang, W. Dong, G. Cui, Y. Zhao, X. Shi, X. Xia, B. Tang, and W. Wang. *RSC Adv.*, **7**(2017):23699–23708. DOI: https://doi.org/10.1039/C7RA02423A.

[83] M. F. Hanafi and N. Sapawe. *Mater. Today*, **31**(2020)(1):260–262, . DOI: https://doi.org/10.1016/j.matpr.2020.05.746.

[84] S. Gorduk, O. Avciata, and U. Avciata. *Inorganica Chimica Acta*, **471**(2018):137–147. DOI: https://doi.org/10.1016/j.ica.2017.11.004.